4

The highest-frequency detection of a radio relic: 16-GHz AMI observations of the 'Sausage' cluster

We observed the cluster CIZA J2242.8+5301 with the Arcminute Microkelvin Imager at 16 GHz and present the first high radio-frequency detection of diffuse, non-thermal cluster emission. This cluster hosts a variety of bright, extended, steep-spectrum synchrotron-emitting radio sources, associated with the intra-cluster medium, called radio relics. Most notably, the northern, Mpc-wide, narrow relic provides strong evidence for diffusive shock acceleration in clusters. We detect a puzzling, flat-spectrum, diffuse extension of the southern relic, which is not visible in the lower radio-frequency maps. The northern radio relic is unequivocally detected and measures an integrated flux of 1.2 ± 0.3 mJy. While the low-frequency (< 2 GHz) spectrum of the northern relic is well represented by a power-law, it clearly steepens towards 16 GHz. This result is inconsistent with diffusive shock acceleration predictions of ageing plasma behind a uniform shock front. The steepening could be caused by an inhomogeneous medium with temperature/density gradients or by lower acceleration efficiencies of high energy electrons. Further modelling is necessary to explain the observed spectrum.

Stroe, Rumsey, Harwood et al.
MNRAS, 441, L41 (2014)

4.1 Introduction

Radio relics are diffuse, strongly-polarised, Mpc-wide synchrotron objects found at the periphery of disturbed galaxy clusters (e.g. Feretti et al. 2001). Relics are thought to trace large-scale, fast, outward-travelling shock fronts (Mach numbers up to 4) induced by major mergers between massive clusters (Ensslin et al. 1998; Sarazin 2002; Feretti et al. 2012). These objects usually extend perpendicularly to the merger axis of their host cluster and display narrow transverse sizes, resulting from a spherical-cap-shaped regions of diffuse emission seen side-on in projection (Feretti et al. 2012). Integrated radio spectral indices of elongated relics below < 1.2 GHz range between $-1.6 < \alpha < -1.0$ ($F_\nu \propto \nu^\alpha$) and the spectra display no curvature up to ~ 2 GHz (Feretti et al. 2012). Ensslin et al. (1998) suggest relics are formed through the diffusive shock acceleration mechanism (DSA; e.g., Drury 1983). In this scenario, intra-cluster-medium (ICM) particles are accelerated by shocks to relativistic speeds in the presence of μG level magnetic fields at the outskirts of clusters (e.g. Bonafede et al. 2009, 2010). Due to low acceleration efficiencies, mildly-relativistic (rather than thermal) electrons likely cross the shock surface multiple times by diffusing back through the shock after each passage. These re-accelerated electrons then exhibit synchrotron radio emission.

CIZA J2242.8+5301 ('Sausage' cluster; Kocevski et al. 2007; van Weeren et al. 2010) hosts a remarkable example of double, Mpc-wide, narrow radio relics. Twin relics are thought to form after a head-on collision of two roughly equal-mass clusters (Roettiger et al. 1999). The northern relic (RN) is bright (0.15 Jy at 1.4 GHz) with an integrated spectral index between 153 MHz and 2.3 GHz of $\alpha_{\rm int} = 1.06 \pm 0.04$ (Stroe et al. 2013). RN displays spectral index steepening and increasing curvature from the outer edge of the relic towards the inner edge, thought to be due to synchrotron and inverse Compton losses in the downstream area of a shock with an injection spectral index of ~ -0.65. The cluster contains a fainter counter-relic towards the south, a variety of diffuse patches of emission and a number of radio head-tail galaxies (Stroe et al. 2013).

Relics have been primarily studied at low radio frequencies (< 1.5 GHz), making accurate determination of the injection, acceleration and loss mechanisms difficult. Most of the ~ 40 radio relics with published spectra (Feretti et al. 2012) have measurements up to 2.3 GHz, while only two relics have spectra derived up to 5 GHz (Abell 521, 2163; Giacintucci et al. 2008; Feretti et al. 2001). The scarcity of high radio-frequency observations of relics is caused by two factors: (i) the steep spectrum means that relics are significantly fainter at high frequencies; (ii) there are few radio telescopes with the required compact uv coverage needed to detect relics. To begin to address this, we performed exploratory observations at 16 GHz with the Arcminute Microkelvin Imager (AMI; AMI Consortium: Zwart et al. 2008) of the 'Sausage' cluster. AMI is the only cm-wavelength radio telescope with the required capabilities for detecting Mpc-wide, low-redshift, diffuse targets at sub-arcminute resolution. In this letter, using two different AMI configurations, we image the 'Sausage' cluster at high (40 arcsec) and low (3 arcmin) resolutions. By combining the data with measurements from the Giant Metrewave Radio Telescope (GMRT) and the Westerbork Synthesis Radio Telescope (WSRT), we derive the RN spectrum over the widest frequency coverage ever performed for a radio relic (between 153 MHz and 16 GHz) and compare our results with predictions from spectral-ageing models. At the redshift of the 'Sausage' cluster, $z = 0.192$, 1 arcmin corresponds to a scale of 0.191 Mpc. All images are in the J2000 coordinate system.

4.2 Observations & Data Reduction

For our analysis, we combine the existing WSRT and GMRT observations with new AMI observations. We use the WSRT and GMRT datasets presented in Stroe et al. (2013) and refer the reader to that paper for details of the data reduction. In summary, the data were flagged, bandpass and gain calibrated and bright sources in the field were removed using the 'peeling' technique (Noordam 2004). A total of three frequencies were observed with the GMRT: 153, 323 and 608 MHz and four with the WSRT: 1.2, 1.4, 1.7 and 2.3 GHz.

4.2.1 AMI observations

AMI is a dual array of interferometers located near Cambridge, UK. The Small Array (SA) and the Large Array (LA), observe over 13.9 – 18.2 GHz and measure the single Stokes polarisation I+Q (AMI Consortium: Zwart et al. 2008). The SA has ten 3.7-m antennas with baselines of 5 – 20 m, while the LA has eight 12.8-m antennas with baselines of 18 – 110 m, giving the instruments sensitivities to complimentary ranges of angular scale. Observations towards the X-ray cluster centre were taken between July 2012 and February 2013 on both SA and LA, with the field observed with a single pointing with the SA and with a series of multi-point hexagonal raster observations on the LA. The northern relic itself was also observed with the LA with four pointings centred along its axis. For all observations, flux calibration was performed using observations of 3C 48, 3C 286 and 3C 147, with 3C 286 calibrated against VLA measurements (Perley & Butler 2013). Raw data were flagged for hardware errors, shadowing and interference and phase and amplitude calibrated using the in-house software package REDUCE (AMI Consortium: Davies et al. 2009). All of the reduced LA data were concatenated into a single uv dataset before mapping.

Unlike the WSRT and GMRT arrays, that measure total intensity I, both AMI arrays measure the single polarisation Stokes I+Q. For the spectral work, it is necessary to correct the AMI values to make them consistent with those from the other telescopes. 4.9-GHz observations (van Weeren et al. 2010) show that RN is 60% polarised and that the magnetic field is tangent to the relic. The measured Faraday depth of -140 rad m^{-2} implies a rotation of 24 degrees between 5 and 16 GHz. We assume the same degree of polarisation at 16 GHz as at 4.9 GHz. AMI calibration assumes random polarisation, which in the case of RN is correct for only 40% of the measured flux. We multiply 60% of the measured I+Q flux by $1/(2\cos^2\phi)$, where ϕ is the angle between the electric field vector and the orientation of the I+Q AMI feeds, which is vertical on the sky. We take into account the variation of ϕ along the relic. The unpolarised RN flux is added to the corrected polarised flux: $I = 40\%(I+Q) + 60\%(I+Q)/(2\cos^2\phi)$. The I integrated flux density is obtained by decreasing 24% from the I+Q value.

4.2.2 Imaging

AMI radio maps

Figure 4.1 shows separate CLEANed maps for the LA and SA data, using 'Briggs' weighting (Robust set to 2.0 to enhance diffuse emission, Briggs 1995). The SA map resolution is 3.0 arcmin ×2.3 arcmin, while the LA has 44 arcsec ×22 arcsec. The RMS noise in the SA

map is $\sim$ 0.1 mJy beam^{-1} near the northern radio relic, while in the LA map it is 35μJy beam^{-1}.

Combining the GMRT, WSRT and the AMI radio maps

To produce directly-comparable, multi-frequency radio images, a number of steps were taken before combining the maps for the study of the integrated spectrum. Due to the very low SA resolution compared to the WSRT and GMRT maps, we chose to combine only the LA map with the other datasets. We imaged the data using the CLEAN algorithm with the same pixel size (1 arcsec per pixel), image size and uniform weighting. The uv-coverage of the LA samples densely down to a uv-distance of 0.8 kλ. Therefore, only GMRT and WSRT data beyond a uv distance of 0.8 kλ were used, so that our radio maps image approximately the same spatial scales on the sky. We simulated an LA observation of a uniform brightness distribution with the angular dimensions of the northern relic as measured by the LA, with the uv coverage and pointings used for the real LA observation. We found that the LA could be resolving out a negligible part of the largest scale diffuse emission. The uv-cut is necessary for extended sources, as inconsistent inner-uv coverages can lead to non-comparable integrated fluxes. All of the maps were primary beam corrected and convolved to the beam of the AMI LA map.

We adopt an absolute flux-scale uncertainty of 10 per cent for the GMRT and WSRT data, following Stroe et al. (2013). This uncertainty results from telescope pointing errors and imperfect calibration. AMI flux scale errors are well-described by 5 per cent of the flux (AMI Consortium: Davies et al. 2011).

4.3 Results

4.3.1 Radio morphologies

SA map

The bottom panel of Figure 4.1 shows a 1.5-GHz WSRT image convolved to the resolution of the SA map, overlaid with SA contours. AMI recovers most of the bright sources detected by WSRT, while the fainter sources are below the noise. Due to the low resolution, sources close to the SA map centre will not only be blended and merged together, but will also have a negative contribution from SZ signal of the cluster. However, because of the excellent uv-coverage at short baselines down to 0.2 kλ, all of the diffuse emission visible at lower frequencies is recovered in the AMI SA map.

The northern relic (RN) displays an arc shape, but the emission is mixed with radio galaxies H and B and diffuse source I (see also top panel, Figure 4.1).

The complex of diffuse emission towards the south of the cluster arises as a blending of sources RS, J, A and tailed-radio source F. At lower frequencies, radio phoenix J is much brighter than the relic RS (Stroe et al. 2013). Since J has a much steeper spectrum than RS, they contribute comparably to the flux at 16 GHz. Puzzling is the $\sim$ 2 mJy integrated flux, 1 Mpc, diffuse extension of RS towards the east, which has no counterpart in the low-resolution WSRT map (see labelling in Figure 4.1). By placing a 3σ upper limit on the WSRT flux (giving $\sim$ 15 mJy), we would expect the spectral index of this extension to be flatter than

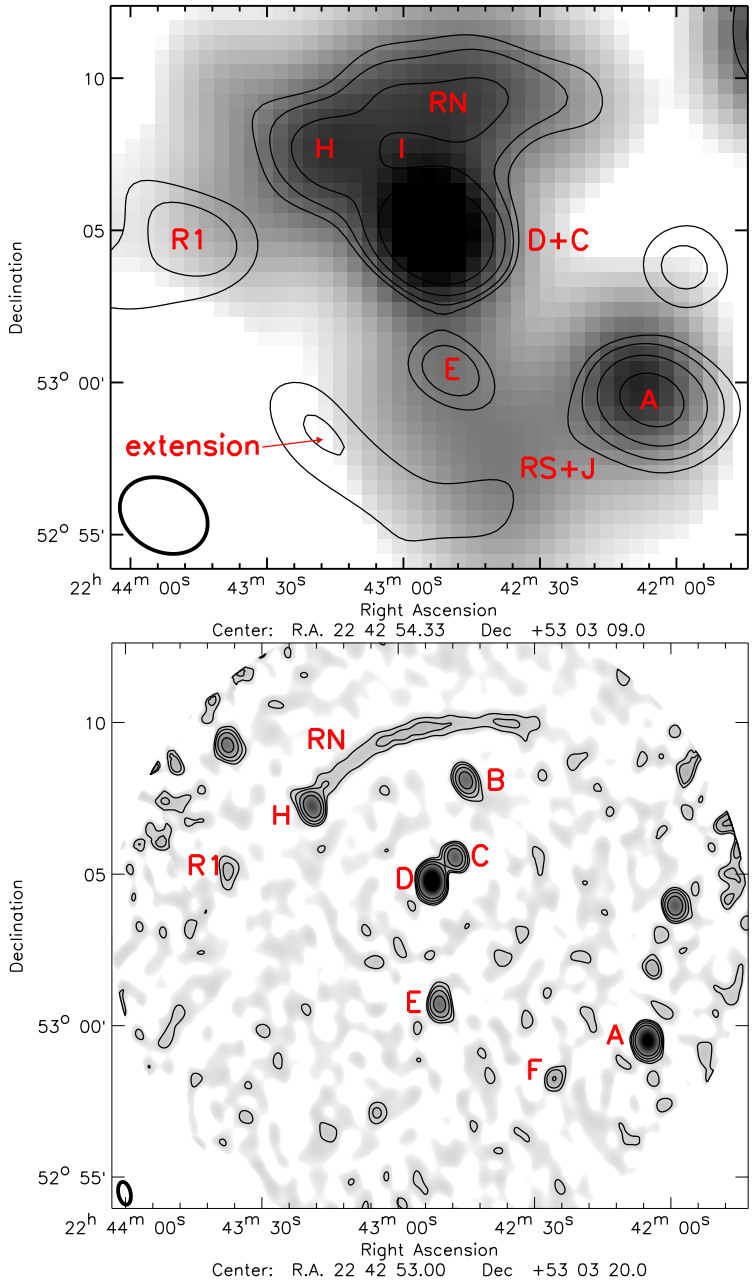

Figure 4.1: 'Briggs'-weighted AMI 16 GHz images (robust=2). Contours drawn at $[4, 8, 16, 32] \times \sigma_{\rm RMS}$. *Top*: AMI SA. The beam size 3.0 arcmin ×2.3 arcmin is shown in the bottom-left corner of the image. The noise is ∼ 0.1 mJy beam^{-1}. The grey intensity shows a low-resolution (3 arcmin) WSRT 1.5 GHz image. *Bottom*: AMI LA in intensity and contours, at 44 arcsec ×22 arcsec resolution, with $\sigma_{\rm RMS} \approx 35\,\mu$Jy beam^{-1}. Source labelling from Stroe et al. (2013) is shown.

−0.5. While the peak in the WSRT emission is towards the west, at the location of compact radio galaxy A, and it progressively wanes towards the east, the AMI SA emission shows the opposite trend. The peak at the emission is located where no counterpart is seen in the WSRT map. There could be some point-source contamination, but this should be minimal as the LA finds no significant sources in the area.

LA map

The top panel of Figure 4.1 shows the AMI LA map (imaged with robust=2). The higher resolution enables a better deblending of sources, but the poorer inner uv-coverage leads to loss of flux on large scales. This is evident as most diffuse sources (RS, J) detected in the SA effectively disappear in the LA map.

The northern relic is detected at the 11σ level at peak flux and clearly separated from its neighbouring source H towards the west. Only the central, brightest part of source R1 is visible. We also detect sources labelled A, B, C, D and E as point sources with high S/N ($> 32\sigma$). The nucleus of tailed-radio galaxy F is detected at 10σ, but its steep spectrum tail is not recovered, as expected (see Stroe et al. 2013). The 'extension' is not detected in the high-resolution 16 GHz, suggesting it may have a diffuse nature.

4.3.2 Integrated spectrum

Figure 4.2 and Table 4.1 present the spectrum of RN. The flux densities are measured in fixed boxes in uniform-weighted maps. Note that because of the uniform weighting, RN is detected at 6σ level significance at peak. We use a least-squares method to fit a single power law to the integrated flux-density of the relic from each of the eight radio maps, at common resolution and with the common uv-cut. This fitting takes into account a total flux error computed as the quadrature of the flux scale error of 10 per cent for the GMRT and WSRT measurements and 5 per cent in the AMI LA, and the RMS noise in each map multiplied by the square root of the number of beams contained in the box we measure the flux in.

From spatially-resolved, low-frequency observations of RN, we found a ~ -0.6 injection index, with an integrated spectrum between 153 MHz and 2.3 GHz well-described by a linear fit with slope -1.06 (Stroe et al. 2013). Figure 4.2 shows in the dotted line the injection spectrum of the freshly-accelerated electrons, while the dashed line presents the integrated spectrum, as derived from the low-frequency data. A single power law fit ($\alpha_{\rm int} = -1.33 \pm 0.03$) provides a poor description of the data up to 16 GHz, as the fitted line fails to pass through all but two error bars, with a reduced $\chi^2_{\rm red}$ of 163 (solid line in Figure 4.2). The 16 GHz measurement lies 12σ below the extrapolation of the low-frequency spectrum.

4.4 Discussion

Radio relics are thought to form at the wakes of travelling shock fronts produced by the major merger of galaxy clusters (Feretti et al. 2012). The physical processes underlying their formation, such as the injection and ageing mechanism, can be constrained using high-frequency measurements, which have not been performed until now. Here, we present the 16 GHz measurement of a relic through AMI observations of the 'Sausage' cluster.

Table 4.1: Integrated radio spectrum of the RN measured in the uniform-weighted radio maps with common uv-cut and resolution. The uncertainties of the measurements are computed as the quadrature of the flux error and the rms noise in each map, multiplied by the square root of the number of beams spanned by the source. Note that RN is detected at a total S/N of 24 in the integrated spectrum. Taking the lower bound given by the error in the integrated flux results in a 18σ detection.

Freq. [GHz]	0.15	0.32	0.6	1.2	1.4	1.7	2.3	16
Flux [mJy]	668	270	187	107	96	67	28	1.2
Error [mJy]	69	28	19	11	10	7	3	0.3

4.4.1 Northern relic

The 16 GHz measurement of the northern relic and its integrated spectrum are given in Fig. 4.2 and Table 4.1. We find strong evidence for high-frequency steepening in the integrated spectrum of RN. There are two reasons why this should be considered a robust measurement. Firstly, the integrated spectra of point sources in the GMRT, WSRT and AMI LA maps are well described by single power laws, implying a correct overall flux scale also for the 16 GHz measurements. Secondly, the dense AMI LA uv-coverage at the shortest spacings indicates minimal loss of flux at large spacial scales.

All of the lower-frequency measurements (GMRT and WSRT, < 2.3 GHz) present firm evidence for a scenario where the source traces an outward travelling shock wave. The ICM electrons are accelerated at the shock via the DSA mechanism, resulting in a relatively flat injection spectral index ($\alpha \sim -0.6$; van Weeren et al. 2010; Stroe et al. 2013). Energy losses due to synchrotron and inverse Compton processes lead to spectral index steepening and increasing spectral curvature in the downstream area (van Weeren et al. 2010; Stroe et al. 2013).

Ensslin et al. (1998) modelled the integrated radio spectrum for such a relic formation scenario. At the shock front the particles are accelerated to a power-law radio spectrum, followed by losses that steepen the spectra. The integrated spectrum results from the summation of particle spectra spanning a range of ages from different regions in the downstream area. This is equivalent to the continuous injection model which was proposed to explain the integrated spectra of radio galaxies, where the jet deposits freshly accelerated electron in the radio lobes at a constant rate (CI; Pacholczyk 1970).

In the CI model, the integrated spectrum has a critical frequency $\nu_{\rm crit}$, beyond which the spectrum steepens by 0.5 because of energetic losses (Pacholczyk 1970). Ensslin et al. (1998) follows this approach and assumes that the integrated spectrum is measured beyond this critical frequency (~ 100 MHz), where we observe the aged spectrum. Therefore, simple plane-shock theory in the context of DSA predicts that the relic integrated spectral index of a source should be 0.5 steeper than the injection index of the freshly-accelerated electrons, which has a hard upper limit at -0.5 (Pacholczyk 1970). In Stroe et al. (2013), we showed that the spectral index and curvature maps for the northern relic are consistent with this model. The relic injection index is -0.6, which defines a shock front Mach number of 4.6 ± 1.1 (Stroe et al. 2013). The difference between the injection index ~ -0.6 and the integrated index below 2.3 GHz of -1.06 ± 0.04 is consistent with the prediction from the CI model (Stroe et al. 2013).

However, by extrapolating the RN low-frequency spectrum, we find that the 16 GHz mea-

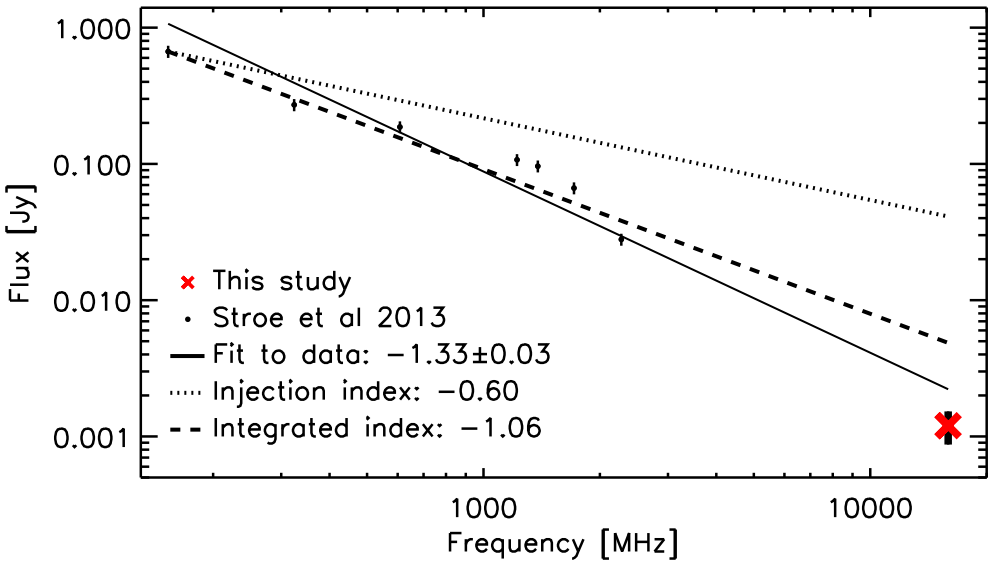

Figure 4.2: Integrated radio spectrum of the northern relic from 153 MHz up to 16 GHz (see also Table 4.1). The red cross marks the 16 GHz measurement. The uncertainties include a 10 per cent flux scale error added in quadrature to the $\sigma_{\rm RMS}$. A power-law is fitted to the eight frequencies. The dotted line shows the injection spectrum and the dashed line the integrated spectrum, as derived from high-resolution GMRT and WSRT data (Stroe et al. 2013). The injection and integrated spectra below 2.3 GHz are consistent with a CI model. The 16 GHz measurement is 12σ below the CI prediction.

surement is in stringent tension with the CI prediction, at the 12σ significance level (see Fig. 4.2). The integrated 153 MHz to 16 GHz index is much steeper (~ 0.8) than the injection index, while if only the high-frequency data is considered, this difference increases to 1.2 spectral index units.

There are several explanations for this discrepancy between the 16 GHz and the lower frequency measurements:

- As mentioned previously, the Ensslin et al. (1998) model only holds for frequencies above the break frequency, where there is a balance between continuously, freshly injected plasma and ageing. In reality, there is a broad frequency range over which the steepening takes place. If the break occurs over a range of frequencies below $\sim$ 100 MHz, then the steepening would gradually increase towards higher frequencies, giving a curved integrated spectrum, as the one we observe in the northern relic. In cases where the spectral break occurs across the observed frequency range, the results will be biased to flatter integrated spectra and hence stronger derived Mach number.

- The injection spectrum is not a power law. With a pool of thermal or pre-accelerated electrons, the injection spectrum is still expected to be a power law (Brunetti & Jones 2014). The acceleration efficiency for electrons beyond $\gamma \approx 3 \times 10^4$ Lorentz factors (equivalent to a few GHz-peak emission frequency for μG magnetic fields) might be

smaller than for the lower energy electrons. During their multiple crossings of the shock front, the electrons lose energy and radiatively cool during the acceleration, leading to a curved injection spectrum, assuming that the electron mean free path is larger than its gyro-radius (Keshet et al. 2003).

- A gradient of density and/or temperature across the source would result in different spectral components, resulting in a 16-GHz spectrum completely dominated by losses/aged electrons. Assuming an isothermal sphere ICM gas distribution (Sarazin 2002), we calculate a drop of 15 – 25 per cent in electron gas density across the 50 – 100-kpc width of the northern relic. The outward-movement of the shock, from regions of higher densities into lower densities, suggests that, in the past, the shock was crossing a region of higher electron density. The shock might have injected a larger pool of electrons in the past, compared to now. When summing up the particle spectra, the older electrons would have a higher normalisation, hence larger weight in the integrated spectrum. Therefore, the integrated spectrum would be dominated by the heavily-curved spectrum of the aged electrons.

- The magnetic field at the shock location might be stronger than in the downstream area, as a result of shock compression. Acceleration in the presence of ordered, strong magnetic fields at the shock front, combined with turbulent, lower magnetic fields in the downstream area, could lead to a curved integrated spectrum. Simulations of supernova remnant synchrotron emission under turbulent magnetic field conditions suggest that electrons in the cut-off regime can radiate efficiently (Bykov et al. 2008).

Nevertheless, higher-resolution data is required for distinguishing between these scenarios. At the moment, no relic formation mechanism can readily explain the high-frequency steepening, thus new theoretical models have to be developed (Brunetti & Jones 2014).

4.4.2 Diffuse extension

Towards the south of the cluster, we discover an extension at the 8σ significance level towards the east of RS in the low-resolution SA AMI map. This source does not have a counterpart in the lower frequency data, or in the high-resolution AMI LA map (Figure 4.1), excluding the possibility of a point source. The extension appears elongated ($\sim$ 1 Mpc) and has a spectrum flatter than ~ -0.5. Its arc-like shape and proximity to RS make the extension an ideal candidate for a relic, but its flat integrated spectral index means that the source cannot result from a shock front in the context of DSA. Striking also is the difference between the spectral index of the extension and RS, which points to very different shock properties towards the south and towards the south-west. This could be explained by different ICM temperature/densities in the two directions. Ogrean et al. (2013) measured a sharp increase in ICM temperature in the direction of this extension, followed by a putative shock with a Mach number of 1.2, coincident with the location of the radio extension. Such an increase in temperature in the downstream area of travelling shock fronts has been also found in simulations (Roettiger et al. 1997). The source seems to trace an arc-like shock front, which suggests a shock seen in projection onto the plane of the sky, which means the radio emission detected is a mixture of different age-populations of electrons.

4.5 Conclusions

High radio-frequency observations of steep-spectrum, diffuse, cluster emission have not previously been made owing to a lack of suitable instrumentation. We have observed the 'Sausage' merging cluster at 16 GHz at low (3 arcmin) and high (40 arcsec) resolution with the AMI array and we successfully detect diffuse radio relic emission for the first time at frequencies beyond 5 GHz. Our main results are:

- The northern relic measures an integrated flux density of 1.2 ± 0.3 mJy (6σ peak detection in a uniformly-weighted map). We investigate in detail its integrated spectrum and conclude there are clear signs of spectral steepening at high frequencies. If thermal electrons are accelerated, the steepening can be caused by a lower acceleration efficiency for the high-energy ($\gamma > 3 \times 10^4$) electrons, a negative ICM density/temperature gradient across the source or turbulent downstream magnetic fields amplifying the emission of electrons in the cut-off regime. However, these scenarios are unlikely because of low-acceleration efficiencies at weak-Mach-number shocks. Further theoretical modelling is required.

- We also detect a peculiar, flat-spectrum ($\alpha_{\rm int} \approx -0.5$) patch of diffuse emission towards the south-east of the cluster, which cannot be explained by the CI model.

The surprising high-frequency spectral steepening results and flat-spectra presented here suggest that the simple CI model, which has been widely used in the literature to explain the formation of radio relics, needs to be revisited. Furthermore, there is a clear need for high-quality radio observations of relics at cm and mm-wavelengths that resolve radio relics.

Acknowledgements

We thank the referee for the comments which greatly improved the clarity and interpretation of the results. We also thank Gianfranco Brunetti, Tom Jones, Martin Hardcastle, Andrei Bykov, Matthias Hoeft, Wendy Williams and Marja Seidel for useful discussions. We thank the staff of the Mullard Radio Astronomy Observatory for their invaluable assistance in the operation of AMI, which is supported by Cambridge University. This research has made use of the NASA/IPAC Extragalactic Database (NED) which is operated by the Jet Propulsion Laboratory, California Institute of Technology, under contract with the National Aeronautics and Space Administration. This research has made use of NASA's Astrophysics Data System. AS acknowledges financial support from NWO. CR acknowledges the support of STFC studentships. JJH thanks the University of Hertfordshire and the STFC for their funding. RJvW is supported by NASA through the Einstein Postdoctoral grant number PF2-130104 awarded by the Chandra X-ray Center, which is operated by the Smithsonian Astrophysical Observatory for NASA under contract NAS8-03060. DS is supported by a VENI fellowship. YCP acknowledges the support of a Rutherford Foundation/CCT/Cavendish Laboratory studentship.

Bibliography

Davies, M. L., Franzen, T. M. O., Davies, R. D., et al. 2009, MNRAS, 400, 984

AMI Consortium, Davies, M. L., Franzen, T. M. O., et al. 2011, MNRAS, 415, 2708

AMI Consortium, Zwart, J. T. L., Barker, R. W., Biddulph, P., et al. 2008, MNRAS, 391, 1545

Bonafede, A., Feretti, L., Giovannini, G., et al. 2009, A&A, 503, 707

Bonafede, A., Feretti, L., Murgia, M., et al. 2010, A&A, 513, A30

Briggs, D. S. 1995, PhD thesis, New Mexico Tech, USA

Brunetti, G., & Jones, T. W. 2014, arXiv:1401.7519

Bykov, A. M., Uvarov, Y. A., & Ellison, D. C. 2008, ApJL, 689, L133

Dressler, A. 1980, ApJ, 236, 351

Drury, L. O. 1983, Reports on Progress in Physics, 46, 973

Ensslin, T. A., Biermann, P. L., Klein, U., & Kohle, S. 1998, A&A, 332, 395

Feretti, L., Fusco-Femiano, R., Giovannini, G., & Govoni, F. 2001, A&A, 373, 106

Feretti, L., Giovannini, G., Govoni, F., & Murgia, M. 2012, A&Ar, 20, 54

Giacintucci, S., Venturi, T., Macario, G., et al. 2008, A&A, 486, 347

Keshet, U., Waxman, E., Loeb, A., Springel, V., & Hernquist, L. 2003, ApJ, 585, 128

Kocevski, D. D., Ebeling, H., Mullis, C. R., & Tully, R. B. 2007, ApJ, 662, 224

Noordam, J. E. 2004, in SPIE Conference Series, Vol. 5489, ed. J. M. Oschmann, Jr., 817–825s

Ogrean, G. A., Brüggen, M., Röttgering, H., et al. 2013, MNRAS, 429, 2617

Pacholczyk, A. G, 1970, Radio astrophysics

Perley, R. A., & Butler, B. J. 2013, ApJS, 204, 19

Roettiger, K., Loken, C., Burns, J. O., 1997, ApJS, 109, 307

Roettiger, K., Burns, J. O., & Stone, J. M. 1999, ApJ, 518, 603

Sarazin, C. L. 2002, in Astrophysics and Space Science Library, Vol. 272, 1–38

Stroe, A., van Weeren, R. J., Intema, H. T., et al. 2013, A&A, 555, A110

van Weeren, R. J., Röttgering, H. J. A., Brüggen, M., & Hoeft, M. 2010, Science, 330, 347